Journal of Alloys and Compounds 506 (2010) 179–187

Contents lists available at ScienceDirect

Journal of Alloys and Compounds

journal homepage: www.elsevier.com/locate/jallcom

Structure and consolidation of rapidly solidified Meso 10 alloy flakes

L. Blaz [a,*], M. Sugamata [b], G. Wloch [a], J. Sobota [a], A. Kula [a]

[a] AGH-University of Science and Technology, Department of Structure and Mechanics of Solids, Cracow, Poland
[b] Nihon University, College of Industrial Technology, Tokyo, Chiba, Japan

ARTICLE INFO

Article history:
Received 3 February 2010
Received in revised form 25 June 2010
Accepted 30 June 2010
Available online 7 July 2010

Keywords:
Powder metallurgy
AA7000 aluminum alloy
Rapid solidification
Extrusion
TEM
SAD pattern analysis
Quasicrystals

ABSTRACT

Hot compression tests were carried out on rapidly solidified (RS) and KOBO-extruded Meso10 alloy (AA7000 series), in a range of temperatures between 293 K and 773 K. The flow stress was higher than that of as-extruded industrial 7N01 alloy with a composition close to AA7039. Structural observations revealed an uncommon structure of the rapidly solidified Meso 10 alloy. Fine Zn-rich particles, 20–180 nm in size, were observed in RS-flakes. The crystallographic structure of the particles does not resemble the structures of η′, η, or T-phases that are commonly reported for age–hardenable AA7000 series alloys. Hot deformation and prolonged ageing of as-extruded material result in a transformation of the RS structure into one that is typical for AA7000 series alloys. For comparison, structural observations on RS-material produced by commonly used direct hot-extrusion that involves the preheating of the charge at 673 K were also performed. Effect of the processing path on materials properties is discussed.

1. Introduction

Commonly used methods for effective strengthening of industrial aluminum alloys are mostly based on the grain size refining combined with ageing and strain hardening procedures. The most sophisticated technologies of structural hardening of the alloys include the powder metallurgy and mechanical alloying (MA) of Al-based composites. In particular, a very pronounced hardening effect is observed for Al- and Al–Mg alloy-based MA composites reinforced with very fine powders of metal oxides and silicides [1–4]. However, MA methods are relatively expensive and time-consuming procedures that result in very limited application of the method in industrial practice.

Relatively efficient production of bulk materials with refined structures is based on rapid solidification methods. Rapid solidification (RS) of aluminum alloys, combined with mechanical consolidation of RS powders, is an attractive metallurgical procedure on account of its sufficiently high efficiency and the effective refining of structural components. When utilizing this method, production costs may be lowered significantly. The mechanical consolidation of RS powders is usually performed by preliminary pressing of RS powder, vacuum degassing, and then hot extrusion of as-compressed metallic charge. A major problem encountered when using the method is the influence of temperature on the coarsening of structural components during both preliminary heating of the charge and high-temperature processing of the material. The most promising results on the production of nano-structured RS alloys and MA metallic composites can be obtained for the materials characterized by sufficiently high-temperature stability of reinforcements. For example, primary Si-particles and eutectic silicon in RS hypereutectic aluminum–silicon alloys, processed by means of commonly used powder metallurgy (PM) methods, were found to be very stable during both powder hot consolidation and heat treatment procedures, as well as hot deformation tests [5–8]. Furthermore, SiC whiskers (SiC_w) and SiC nano-particles (SiC_p) are not susceptible to the coarsening during high-temperature processing and heat treatment of aluminum- and aluminum/magnesium-based composites [9–13].

The improvements offered by RS methods are associated with the refinement of structural components, enlarged solid solubility, reduced segregation of alloying elements and advantageous morphology of intermediate and constitutive phases. In particular, zinc content in AA7000 aluminum alloys is in practice limited to about 8% for conventional cast materials because of inherent foundry problems related to solute segregation and cracking. By reducing the segregation of zinc and making the distribution of phases more homogeneous, rapid solidification of the alloys makes it possible to increase zinc content, which, in consequence, increases the strength of the material [14].

It could be assumed that the rapid solidification of the precipitation–hardenable alloys facilitates the ageing of the material immediately after solidification. However, the age hardening

* Corresponding author.
E-mail address: blaz@agh.edu.pl (L. Blaz).

0925-8388/$ – see front matter © 2010 Elsevier B.V. All rights reserved.
doi:10.1016/j.jallcom.2010.06.173

Table 1
Crystallographic parameters reported in literature for some hardening phases in AA7000 series.

Type	Structure	Parameters in nm		Reference
		a	*c*	
η'	Hexagonal	0.496	0.868	Mondolfo et al. cited in Ref. [14]
	Hexagonal	0.489	1.374	Auld and Cousland cited in Ref. [14]
	Hexagonal	0.496	1.403	Graf cited in Ref. [14]
	Monoclinic	0.497 ($b=a$)	0.554 ($\gamma=120^\circ$)	Gjonnes and Siemensen [21] cited in Ref. [14]
	Hexagonal	0.489 ($d_{10.0\eta'} \approx 3d_{220Al}$)	1.374 ($d_{00.1\eta'} \approx 6d_{111Al}$)	De Sanctis [14] and Salamci [17]
η' (R)	Hexagonal	0.496	0.702	[1]
η_2' (R_2)	Hexagonal	0.496	0.554	[1]
η	Hexagonal	0.521	0.860	Laves cited in [14]
η_{1-11}	Hexagonal	0.515–0.523	0.848–0.862	[1]
T′	Cubic	1.42–1.44	–	[1]
	Hexagonal	1.39	2.75	
T	Cubic	1.416–1.429	–	[1]
Al–Cu–Mg phases				
S″, S′	Orthorhombic, or monoclinic	$a=0.400–0.405$ $b=0.905–0.925$ $c=0.718–0.724$		[1]
S	Orthorhombic	$a=0.400–0.404$ $b=0.923–0.925$ $c=0.714–0.717$		[1]
S	Orthorhombic	$a=0.401$ $b=0.935$ $c=0.715$		[1]

effectiveness depends on RS conditions, as well as the temperature at which the ensuing RS-powder/flakes consolidation and processing are performed. For example, De Sanctis [14] and Salamci and Cochrane [15,16] presented an efficient industrial OSPRAY® method for the production of AA7000 series RS bulk materials. The method is based on spray atomization of the liquid alloy and direct spray solidification on intensively cooled solid substrate. Spray depositioning conditions must be carefully controlled in order to retain a very thin liquid layer on the surface of the spray-deposited preform that is necessary for efficient bounding of fine droplets. However, the supersaturation of as-received RS solid solutions was not sufficiently effective as far as the ageing of the as-deposited perform was concerned. Therefore, the authors of the above-mentioned papers performed additional solution treatment of the RS-material before its final ageing.

The morphology of particles and the type of dominant phases in commercial AA7000 series products depends on the alloy composition and manufacturing conditions [1,5,14–21]. For example, the most commonly observed particles in commercial AA7050, quenched from various temperatures, are: the orthorhombic S-phase Al_2CuMg that is formed at 573–713 K, with the maximum fraction at 683 K; the hexagonal η-phase $Mg(Zn_2,AlCu)$ formed below ~713 K, with the maximum fraction observed below 483 K. Prolonged annealing results in the development of the T-phase $Al_{32}(Mg,Zn)_{49}$ [18]. In the majority of commercial alloys, some insoluble constituent phases, for instance Al_7Cu_2Fe, are also observed. However, their contribution to the hardening of the material is related to the grain coarsening retardation rather than the precipitation–hardening effect.

The ageing of solution-treated AA7000 materials results in effective precipitation–hardening due to the development of metastable phases. The sequence of precipitation mostly depends on ageing temperature and composition of the alloy. Precipitation at low ageing temperatures (<460 K) usually follows the commonly known sequence: supersaturated solid solution (sss) → Guinier–Preston (GP) zones (spherical) → η' metastable phase $Mg(Zn_2,AlCu)$ (plate-like) → η-phase $MgZn_2$ or $Mg(Zn_2,Al,Cu)$ → T-phase reported as $Al_{32}(Mg,Zn)_{49}$ [1,18,19] or $(Al,Zn)_{49}Mg_{32}$ [1,17,15,14] or $Al_2Mg_3Zn_3$ [1]. Particles of η' and η hexagonal phase ($MgZn_2$) are usually observed at AA7000 alloys at relatively high Zn/Cu,Mg ratios. Solid solution decomposition is accompanied by fine η' and then η plate-like particles' growth, which results in the maximum hardening typical for T6 treatment conditions. It is worth mentioning that a series of orientation relationships between the η-phase and the matrix were reported, which resulted in the designation of given η-particle with a subindex [1].

Multi-step precipitation was widely investigated for solution-treated and aged Al–Zn–Mg alloys containing Zn/Mg ratios close to the stoichiometry of the $MgZn_2$ phase [21–25]. Ageing within the temperature range of 323–473 K was reported to result in the development of GP zones that precede the dispersed nucleation of the η'-transition phase and the $\eta' \rightarrow \eta(MgZn_2)$ transformation. Spherical GP zones are usually formed below 323 K, and they are practically stable during the initial stage of ageing [21,22,25]. On the other hand, GP zones are completely eliminated during the second step ageing sequence at 423 K as they become directly transformed to η' and η-particles [21]. Prolonged ageing above 463 K results in the development of the ternary cubic T-phase formed from pre-existing η-precipitates.

The detailed analysis of η'-particles revealed several types of particles varied in shape. Polygonal plates or fine rods of η' have different matrix/particle relations. Plate-like particles of η' are coherent with the matrix on the $(1\,1\,1)_{Al}$ planes, $d_{1\,0\,\bar{1}\,0\eta'} = 3d_{2\,2\,0\,Al}$ [14]. The η'-particles reach up to 20 nm in diameter and 3 nm in thickness, and usually maintain the orientation relationship of $(0\,0\,0\,1)_{\eta'} \| (1\,1\,1)_{Al}$; $[1\,1\,\bar{2}\,0]_{\eta'} \| [1\,1\,2]_{Al}$ [14,23]. Gjonnes and Simensen [21] distinguished at least nine different Al-matrix vs. η'-particle lattice relationships that correspond to particles of various shapes. A unit cell with dimensions $a=0.497$ nm and $c=0.554$ nm for η'-hexagonal lattice was reported for all the investigated types of particles.

The coarsening of η'-particles is accompanied by an increase in internal order upon prolonged ageing. The transformation of η' into η was observed when the particle size reached a size of approximately 20 nm. The composition of both $\eta'$and η is very close to $MgZn_2$. Lattice parameters for the $MgZn_2$ phase (η) are slightly different for η-particles observed for various compositions of Al–Zn–Mg alloys [21].

Table 2
Chemical composition of Meso 10 alloy.

Element	Zn	Mg	Cu	Fe	Si	Mn	Ag	Al
wt.%	9.50	2.97	1.72	0.007	0.013	Traces	0.052	In balance

It is worth mentioning that the literature data are not consistent and other crystallographic structures are also reported, in particular for η'. For the purpose of comparison, some literature data for η' and η-phases are shown in Table 1.

In spite of some discrepancy between crystallographic data and morphology of specific particles reported for aged AA7000 series alloys, the effects of solution time/temperature conditions and the cooling rate are commonly considered to be important factors for industrial heat treatment procedures. The careful selection of solution treatment temperature/time conditions, which depends on the chemical composition of the alloy, is of particular importance. Prolonged solution treatment of the alloys results in undesirable changes of the material's properties, mostly due to grain coarsening. Solution treatment is therefore often performed just below the *solvus* temperature in order to keep the grain boundary pinned by some incompletely dissolved particles, and in this way reduce grain coarsening.

In order to reduce the grain size in precipitation–hardenable alloys, the attention was focused on powder metallurgy technologies (P/M) combined with rapid solidification. The method provides effective reduction of the grain size and refining of the constitutive phases, as well as solid solution oversaturation, which should enable additional hardening during the ensuing ageing of RS-material.

However, the issue of consolidation of nano-structured RS or MA powders into bulk engineering materials usable for many practical applications carries with it the challenge of researching new methods that would allow to maintain the very fine structure of RS powders during processing.

A critical issue in P/M methods is related to the coarsening of the material structure at high-temperature consolidation and processing of RS-materials. It is a rather obvious statement that maintaining a refined structure requires the consolidation temperature to be as low as possible.

To fulfil the above-mentioned requirement, experiments on the consolidation of the RS Messo 10 aluminum alloy powders (AA7000 series) were performed by means of the reversible oscillating die extrusion method (KOBO) [26–28]. This method offers the advantage of using a low processing temperature and omitting the charge preheating procedure before extrusion, even if a high extrusion ratio is used. Even if a heating pulse occurs due to intense deformation, its duration is likely to be too short to cause the coarsening of the fine RS structure.

Nano-structured bulk materials, synthesized through different processes, often vary significantly in terms of their mechanical properties, which is attributed to the variance in microstructural features, defects, flaws and porosity levels [29,8]. Using high extrusion ratios and intense deformation that are available with the KOBO method, effective homogenization of the processed material is possible.

2. Experimental

Experiments were performed on the Meso 10 alloy with similar composition to AA7049, but with slightly increased zinc content. Rapid solidification of RS-flakes and preliminary vacuum hot compression of RS-flakes were performed at Nihon University. Extrusion of as-compressed material, by means of a KOBO method, as well as TEM/EDX/STEM structural studies, DSC analysis and hot compression tests were performed at AGH-University of Science and Technology.

3. Material

The chemical composition of the Meso 10 alloy is shown in Table 2. The alloy was melted above *liquidus* temperature and spray-deposited on an intensively cooled rotating copper cylinder. High-pressure argon gas was used for the melt atomization in an inert gas atmosphere. The obtained fine flakes, less than 0.3 mm thick, were preliminarily compressed in AA6061 cans. Consolidation of RS-flakes via vacuum compression was then performed at ~670 K using 100-ton press. As-compressed billets, 40 mm in diameter, were extruded using oscillating die extrusion (KOBO method) without any preheating of the charge before processing. Rods 7 mm in diameter were extruded at $\lambda = 19$ and at an extrusion rate of 30–60 cm/min. As the material temperature rose due to intense deformation, the rods were water-cooled immediately at the die outlet to avoid coarsening of the structure. Samples for compression tests, 10 mm long and 6 mm in diameter, were machined from the as-extruded rods. Hot compression tests were performed at temperatures between 293 K and 773 K using constant true strain rate of $5 \times 10^{-3}\ s^{-1}$.

To compare the effect of preheating temperature on the structure of as-extruded Mezo 10 alloy selected studies of the rods extruded at 673 K by a common direct hot-extrusion method were also performed. Transmission electron microscopy (TEM) observations revealed the coarsening of preliminary fine Zn-rich particles due to high-temperature processing of the RS-material.

Light microscopy and common techniques for sample preparation were used for preliminary structural observations. The samples were polished using standard metallographic techniques and chemically etched in Tucker's reagent diluted 1:10 in water. TEM observations were performed with a JEM 2010 analytical transmission electron microscope equipped with scanning transmission electron microscopy device (STEM) and Oxford PENTAFET energy dispersive X-ray analysis system (EDX). Thin foils for TEM/STEM observations were prepared using mechanical grinding and ion thinning with a Gatan PIPS 691 machine.

Differential scanning calorimetry experiments (DSC) were performed using a Tolledo TMA/SDTA 840 system. The as-extruded material was tested in the temperature range of 293–973 K and 293–823 K at a heating rate of 30 K/min and 5 K/min respectively. DSC curve was recorded also for the as-melted sample, which simulated the behavior of this material produced by metallurgical methods.

4. Results and discussion

Throughout this article terms such as: "as-extruded" and "KOBO-extruded" material, are used interchangeably to describe material, which was extruded using oscillating die extrusion method without preheating of the charge before processing. The term "hot-extruded" material refers to the material extruded at 673 K by direct hot-extrusion method.

DSC curves for the as-extruded material were analyzed in the temperature range 293–923 K. Two consecutive heating/cooling cycles were performed for the same sample using a constant heating/cooling rate of 30 K/min. Similar tests were repeated at 5 K/min in a lower temperature range (293–823 K) to avoid the melting of the sample. Exothermic effects observed on DSC curves at 450–550 K (Fig. 1), are partly related to the recovery process,

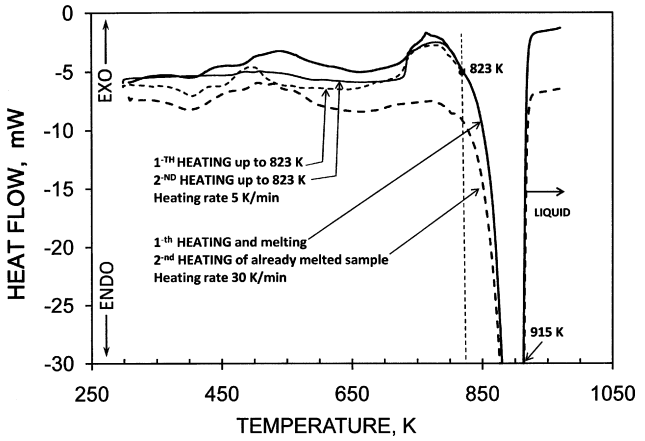

Fig. 1. Heating DSC curves for as-extruded material tested at heating rate 5 K/min within temperature range 293–823 K. For the purpose of comparison, heating at 30 K/min was performed in the 293–973 K range, i.e. up to the melting, in order to compare the DSC curves for as-extruded and re-melted material (Note: "Heating of already melted sample").

which is expected to take place in heavily deformed Al-alloys. As the recovery process does not occur at a re-melted sample, the DSC curve related to the re-melted material shifts below the DSC curves for as-extruded samples. Additional effects, i.e. a slightly marked endothermic effect at 360–420 K and the ensuing exothermic peaks at 450–520 K, are similar to those for the commercial alloy AA7075. In the case of the latter, the low-temperature peak was attributed to the dissolution of GP zones, and the other two peaks to the precipitation of metastable η' and η-phases, respectively [30,31]. The wide depression that occurs at 550–700 K can be attributed to the successive dissolution of particles that finally release the grain boundaries and makes the recrystallization of the matrix at 730–800 K possible (spread exothermic effect). At higher testing temperatures, an enhanced endothermic effect was observed as a result of the melting of the material that started at ~830 K and finished at ~915 K. This last effect is a result of both raising the temperature from *solidus* to *liquidus*, and of the local melting of the material due to some fluctuation in the content of alloying elements in the material volume. Consequently, further hot compression experiments were not performed above 800 K.

The mechanical properties of the as-extruded material were tested at 293–773 K by means of compression tests performed at a constant true strain rate. For the purpose of comparison, a set of samples was annealed at 773 K/30 min and water-quenched before compression.

The typical true stress–true strain curves for the as-extruded material are shown in Fig. 2a. The apparent flow softening at 293 K, observed above $\varepsilon_t \sim 0.25$, was attributed to the growth of fine cracks at high strains. However, complete fracture across the sample was not observed. Initial strain hardening at higher deformation temperatures was followed by steady state flow, which is normally a sign of an intense dynamic recovery process. Sample fracture was not observed within the strain range used in hot compression tests at high deformation temperatures.

The dependence of maximum flow stress on deformation temperature is shown in Fig. 2b. Some data for another industrial alloy (7N01) are also shown for comparison. It is worth emphasizing that dynamic precipitation in the solution-treated (ST) 7N01 industrial alloy, which belongs to the AA7000 series, is evident (see: curve 4 in Fig. 2) [32]. However, the anticipated effect of dynamic precipitation is evidently depressed for both the as-extruded RS Meso 10 alloy and the material solution-treated at 773 K/30 min, and in consequence the characteristics $\sigma_{\max}$ vs. T^{-1} for both as-extruded and solution-treated samples are comparable.

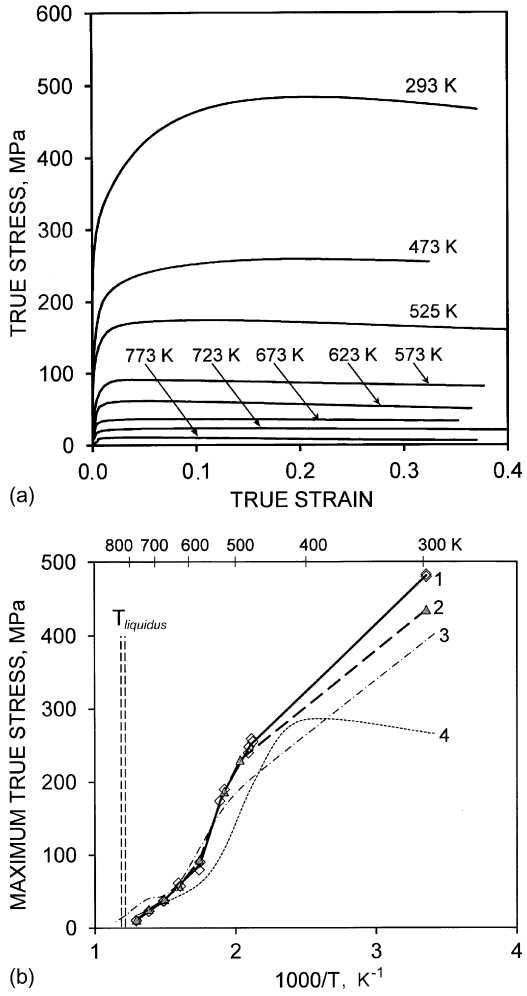

Fig. 2. Results of compression tests performed at constant true strain rate of 5×10^{-3} s^{-1}: (a) flow stress curves for as-extruded Meso 10 alloy (deformation temperatures are marked in the figure); (b) maximum flow stress vs. inverse deformation temperature: (1) as-extruded Meso 10 alloy, and (2) Meso 10 samples preliminarily annealed at 773 K/30 min and water-quenched; (3) as-extruded 7N01 industrial material (AA7000 series) and (4) 7N01 samples preliminarily solution-treated at 743 K/1 h.

4.1. Structural observations

Transverse and longitudinal sections of a KOBO-extruded rod, observed at low magnification, are shown in Fig. 3a. The microstructure was observed on an etched cross-section and transverse sections of the rod, as shown in Fig. 3b and c, respectively. The external layer of the remnant of the AA6061 can cover, and an internal core of gray-shadowed RS-material were distinguished. Only a small number of very fine voids within the highly refined structure were observed. The porosity of the material, roughly estimated using the statistical metallography method, was lower than ~1%.

The decagonal shape of the rod interior (Fig. 3a) resulted from the tenfold symmetry of graved working surface of a die. The AA6061 cover of the rod was removed before machining the samples for further mechanical tests.

Transmission electron microscopy observations were performed in order to investigate the fine structural components of the initial RS-material (flakes), the as-extruded rods and the hot-deformed samples. The structure of the RS flake is shown in Fig. 4a (STEM). It should be emphasized that the observed fine Zn-rich particles were not expected from the cursory analysis of the Al-Zn(Cu,Mg) phase diagram. These particles were not expected for

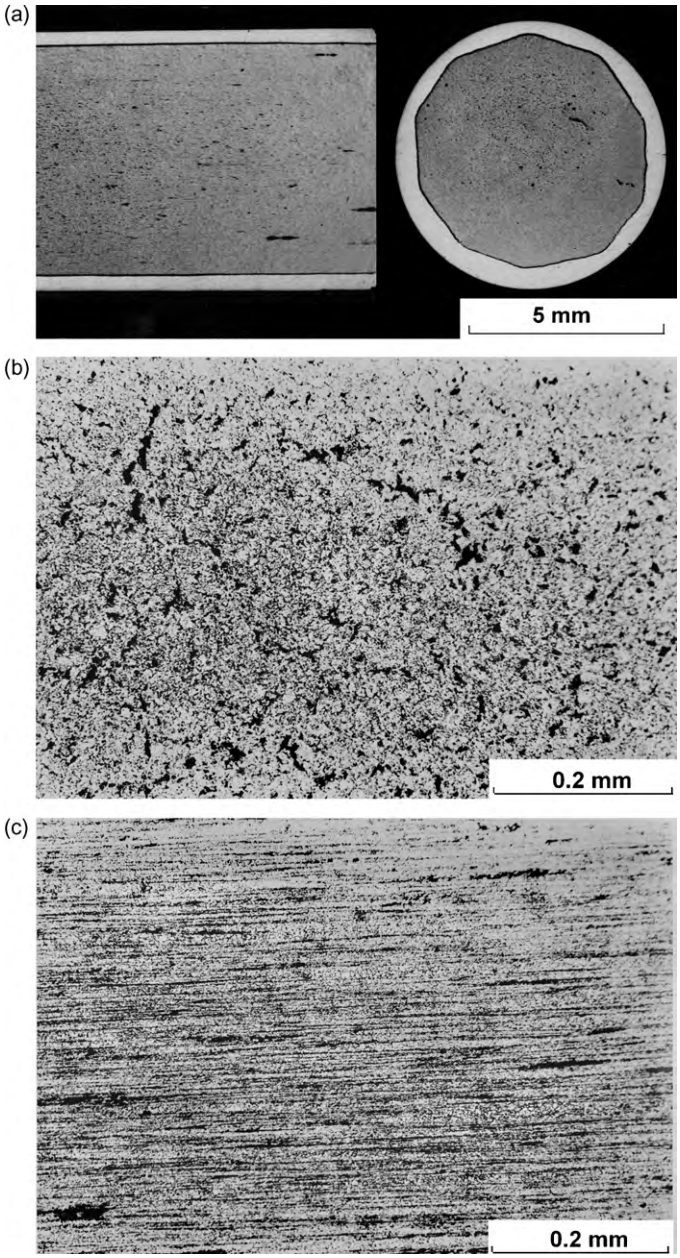

Fig. 3. Structure of as-extruded rod: (a) macro view of longitudinal and transverse section; (b) transverse section; (c) longitudinal section (optical microscopy).

at least two reasons: (1) rapid solidification was performed at a melting temperature higher than the *liquidus* temperature; (2) a large Al(Zn) solid solution area on the diagram suggests that zinc is highly soluble in aluminum at high temperatures. Moreover, the RS procedure was expected to prevent the nucleation of metastable η′ or η-phases and inhibits particle growth to dimensions comparable to those observed in RS-flakes. However, as Gremaud et al. [40], Srivatsan et al. [33], Trivedi et al. [34], had reported earlier, such a large departure from the equilibrium constitution, i.e. identity and composition range of the phases formed, can be observed for some rapidly solidified aluminum alloys.

The chemical composition of particles was investigated by means of TEM/EDX. In order to minimize the effect of Al-matrix radiation on the chemical analysis results, the particles distributed near the edge of the thin foil were analyzed using a beam size of 1–5 nm. The results of the analysis are shown in Table 4. Aluminum was omitted from chemical analyses to better display the atomic stoichiometry of the remaining elements.

TEM observations at sufficiently large magnification revealed a complex structure of quasi-spherical particles. When diffraction contrast was varied during tilting of the sample, very fine nano-sized crystalline components of the particle were revealed (Fig. 4b). Analysis of the obtained SAD pattern points to a complex crystallography of the quasicrystal, which manifests itself in the pattern in a comparable manner to the effect of at least two (or more) overlapping crystal orientations. The SAD pattern, which was typical for threefold symmetry axis, is shown in Fig. 4c. The interplanar distances calculated for spots no. 1–4 were averaged for several patterns and the obtained results are listed in Table 3. Spot no. 1 does not match any axis of η′, η, T-phase or Zn(Al) solid solution structures. The interplanar distances calculated for other spots and the spots symmetry approximately correspond to some orientations of η′ and η-phase, as listed in the table. The differences between interplanar distances reported in literature and the measured values, denoted as *matching error* Δ%, are listed in the table (T–cubic, $a = 14.1$–14.29; η′–hexagonal, $a = 0.496$ nm, $c = 0.702$ nm; η–did not fit any $\{h\,k\,l\}$ combination) [1]. It should be stressed that some similarity of the observed spot distribution to some typical SAD patterns reported for commonly known hardenable particles at AA7000 series is presented solely for the purpose of comparison, and not to ascribe the SAD patterns shown in Fig. 4 to specific phases.

The interplanar distance $d_{2\,2\,0}$ for aluminum is very close to $d_{h\,k\,l}$, measured for spot No. 4. However, attributing the spot to $\{2\,2\,0\}_{Al}$ was not reasonable, since the orientation of surrounding Al-matrix was far away from $[1\,1\,1]_{Al}$ axis. It is worth mentioning that SAD patterns for $[2\,1\,1]_{Al}$ did not reveal additional spots for the η′and η-phases, as reported by Salamci and Cochrane [16], or De Sanctis [14]. While searching for simple symmetry of the particle structure, a tenfold symmetry axis was also revealed. Interplanar distances corresponding to spots 1–4 in Fig. 4d were found to be very close to those marked in Fig. 4c. Tenfold symmetry is typical for quasicrystals enriched with Fe, Cr, Mn, Pd, as reported for some rapidly quenched Al-alloys [35–37]. However, the total composition of Zn-rich particles in the RS Meso 10 flake (Table 4) was similar and did not vary with the observed crystalline symmetry.

Annealing RS-flakes at 773 K/15 min resulted in the transformation of particles into typical structures of η and T-phases, as shown in Fig. 5a. SAD pattern shown in Fig. 5c was taken from the rod-like particle (1) marked in Fig. 5b. Spot distribution corresponded with acceptable accuracy to $\langle 0\,0\,1\rangle_T$ axis ($d_{1\,0\,0} = 1.24$ nm—as measured) for the cubic T-phase ($d_{1\,0\,0} = 1.41$ nm) [1]. Fine particles were identified as η′ or η-type by means of EDX and SAD pattern analyses. The SAD pattern displayed in Fig. 5d corresponds to the hexagonal η′ lattice with the following relationship: $d_{(1\,0\,\bar{1}\,0)} = 0.429$ nm, $d_{(0\,\bar{1}\,1\,1)} = 0.366$ nm, $\alpha = 64.8^\circ$. The corresponding values measured from the SAD pattern, are close to the parameters mentioned above: $d_{h\,k\,l(1)} = 0.458$ nm, $d_{h\,k\,l(2)} = 0.395$ nm and $\alpha = 65^\circ$.

Most of powder metallurgy (PM) methods used in practice, take an advantage of a hot extrusion to produce bulk materials. However, increased temperature results in coarsening of structural components. Therefore, to compare the effect of preheating on the structure of as-extruded Mezo 10 alloy, structural observations of the rod extruded at 673 K by means of a common direct hot-extrusion method are also presented. TEM observations shown in Fig. 6a reveal the coarsening of preliminary fine Zn-rich particles due to high-temperature processing of the RS-material. In spite of a noticeably altered morphology of the particles, EDX analysis did not reveal any remarkable change in their chemical composition. The distribution of alloying components for the material extruded at 673 K is shown in Fig. 6b. The analysis was performed at 50 points

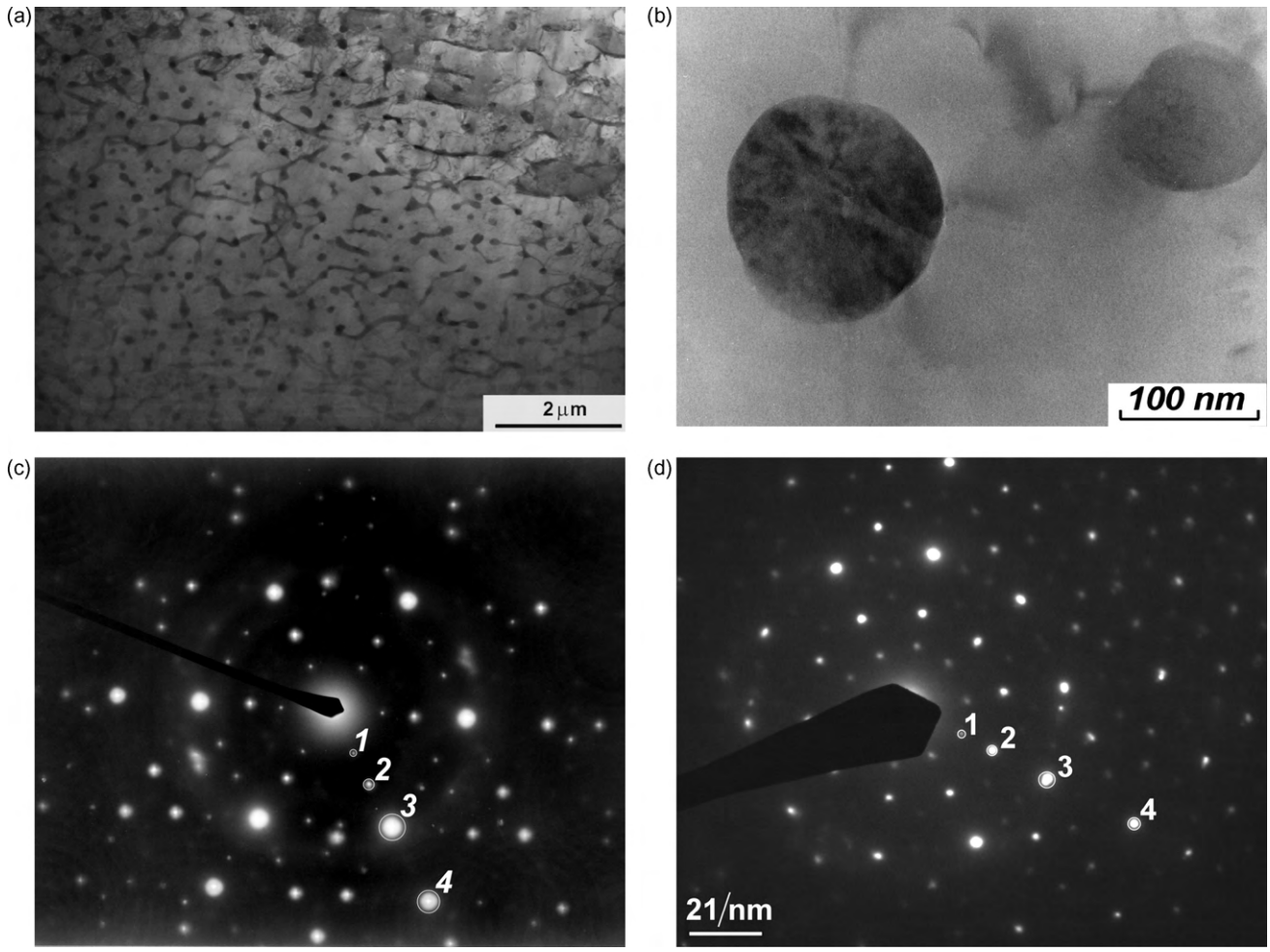

Fig. 4. Structure of RS flake: (a) STEM image; (b) TEM structure of fine particle; (c) SAD pattern taken from a dark particle shown in figure (b); (d) SAD pattern received from another particle that was very similar to these shown in (b). Interplanar distances for the spots marked 1–4 are listed in Table 3.

by equidistant stepping of the electron beam along a line marked in the figure.

In contrary to the hot-extruded material discussed above, relatively low particle coarsening occurs if the oscillating die technique (KOBO extrusion) is used. STEM structure of the material processed by the KOBO method is shown in Fig. 7. When using this method the preheating procedure is omitted and the processing of the material is performed at relatively low temperature. Particle thickness

Table 3
Interplanar distances corresponding to the spots marked in Fig. 4c and d.

Spot no.:	Interplanar distance, d, in nm		
	d_{hkl} measured from SAD pattern, in nm	Corresponding indexes and comparable d_{hkl} values for a common phase (Interplanar angle is close to 60°)	Matching error Δ%
1 (Fig. 4c)	0.616 ± 0.027	No data for η′, η, T-phase were found to fit the spots at $\alpha = 60°$	
2 (Fig. 4c)	0.362 ± 0.005	η′ (0 1 $\bar{1}$ 1) d_{hkl} = 0.366 nm	1.10
		(0 0 0 2) $d_{hk.l}$ = 0.351 nm	−3.04
		$\alpha = 58.5°$	−2.50
		η′ (1 0 $\bar{1}$ 0) d_{hkl}=0.429 nm	−2.50
		(1 0 1 0) d_{hkl} = 0.351 nm	18.51
		$\alpha = 60°$	−3.04
3 (Fig. 4c)	0.226 ± 0.002	η (2 1 $\bar{3}$ 0) d_{hkl} = 0.224 nm	−0.88
		($\bar{2}$ 1 1 0) d_{hkl} = 0.224 nm	−0.88
		$\alpha = 60°$	0
4 (Fig. 4c)	0.139 ± 0.001	Al (0 2 2) d_{hkl} = 0.143 nm	2.88
		(2 0 2) d_{hkl} = 0.143 nm	2.88
		$\alpha = 60°$ (Al-excluded)	0
1 (Fig. 4d)	0.6035 ± 0.0291		
2 (Fig. 4d)	0.3727 ± 0.0059		
3 (Fig. 4d)	0.2304 ± 0.0025		
4 (Fig. 4d)	0.1429 ± 0.0014		

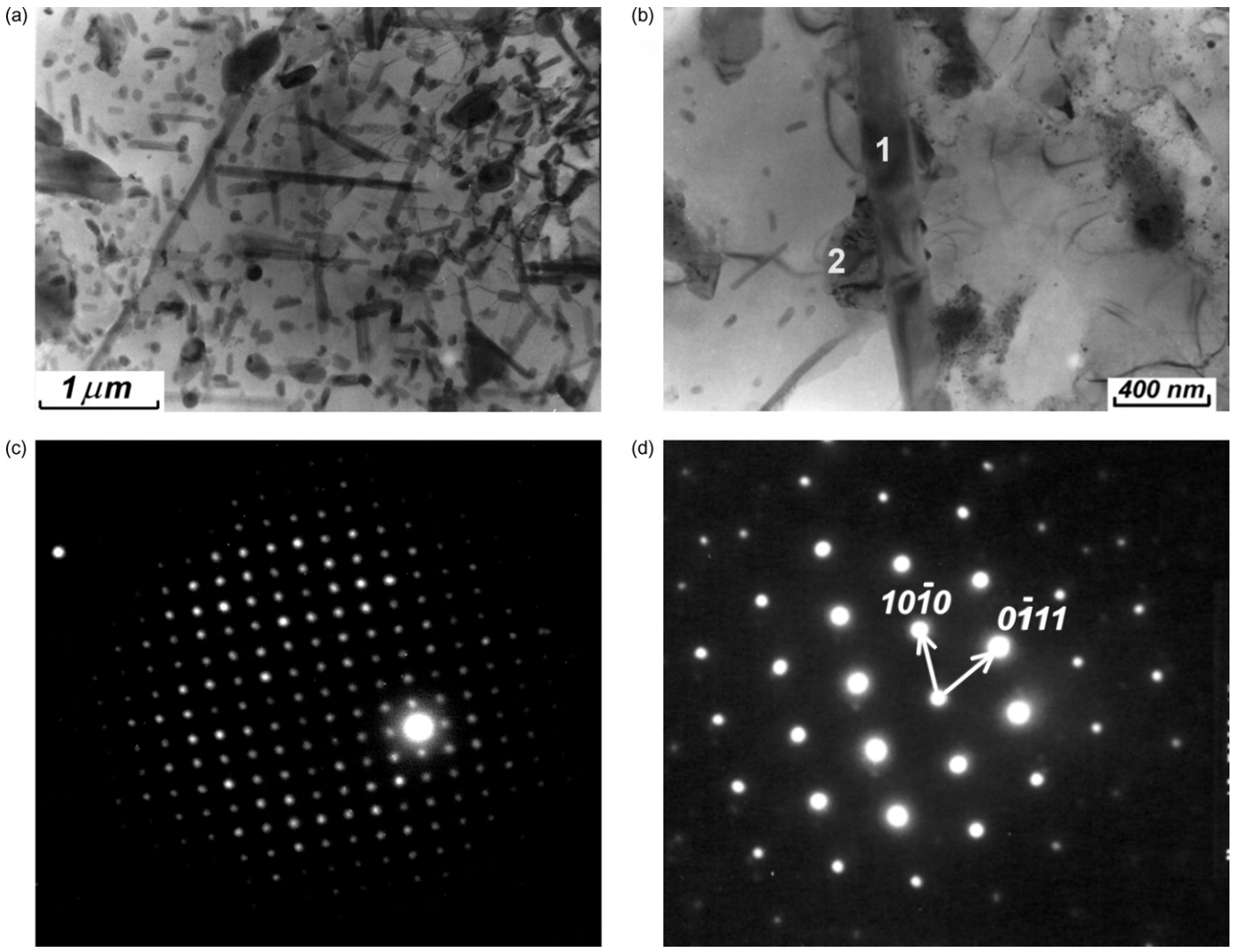

Fig. 5. RS flake annealed at 773 K/15 min: (a) TEM structure; (b) enlarged view of the structure with marked particles that were used for SAD pattern analysis; (c) SAD pattern obtained from rod-like particle (1); (d) SAD pattern obtained from small particle (2).

was measured for as-received RS-flakes, the hot-extruded rod and for the KOBO-extruded material. Over one hundred particles were measured for each sample. The particle size distribution was normalized in order to compare the percentage distribution of the particle size in these materials (Fig. 8). Particle size distribution for the RS flake was not uniform and two particle grades, with maximums at ~20 nm and ~180 nm, were observed. It seems reasonable to conclude that a double maximum in the histogram resulted from the limited area of observations, as well as inheriting the preliminary RS flake structure that was dependent on their initial size and size-dependent cooling rate.

The particle distribution for the RS flake seems to be very similar to that for the KOBO-extruded rod. The most intense coarsening of particles was found for the hot-extruded material at 673 K. The maximum particle size on the last histogram was shifted to ~130 nm.

Table 4
Average content of elements for Zn-rich particles revealed by EDX/TEM analyses near the edge of a thin foil manufactured by ion thinning of as-received RS-flake[a].

	Element content in atomic %			
Element	Zn	Mg	Cu	Mn
Average	46.9	34.7	9.5	8.8
Standard deviation	5.6	6.0	3.4	1.7

[a] EDX analysis was performed for 20 particles. Aluminum content was neglected to omit the matrix radiation effect.

TEM observations were also performed for the selected samples hot-deformed with $\varepsilon_t \sim 0.4$. The samples were water-quenched 1–3 s after deformation had stopped. The most remarkable changes were observed for the solution-treated samples deformed at intermediate deformation temperatures. The structure of the solution-treated sample (743 K/1 h), which was deformed at 573 K, is shown in Fig. 9. Fine η' and η particles observed on the left side of the picture appeared due to dynamic precipitation within the previously recrystallized grain. Heterogeneous nucleation of fine particles at subboundaries and dislocations was evident. It should be emphasized that after solution treatment, the mentioned grain area was free of the original large particles that are typical for RS-material.

The remaining area of the STEM picture (right side of Fig. 9) represents a highly recovered local structure containing large particles. The morphology of the particles indicates unfinished dissolution of preliminary large particles at some area of the material. It seems reasonable to conclude that the time selected for solution treatment was not long enough to complete the particle dissolution necessary to release recrystallization fronts in previously heavily deformed material. Due to enhanced diffusion along the migrat-

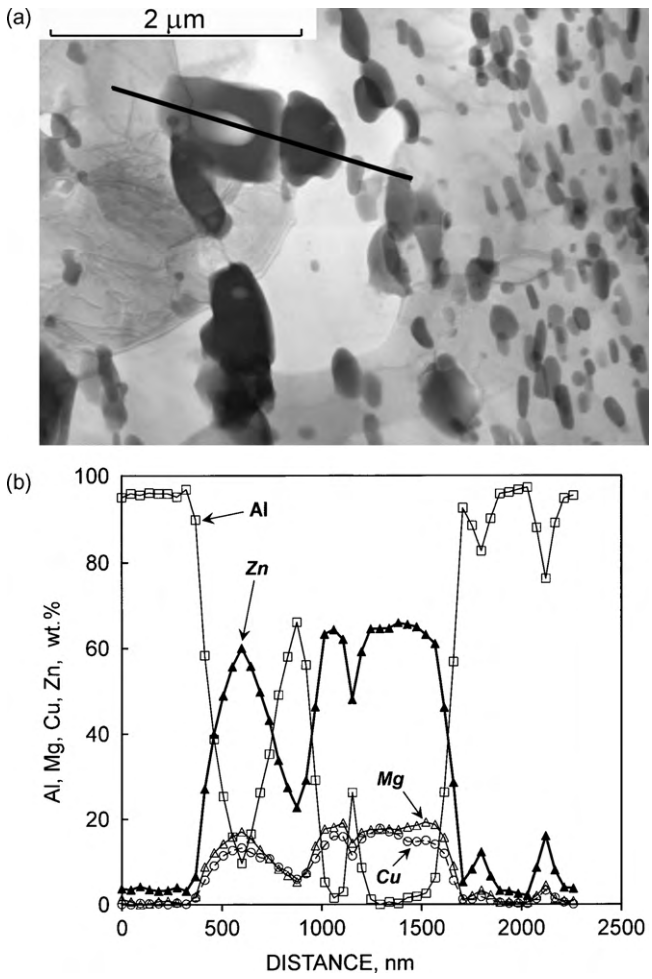

Fig. 6. Structure of hot-extruded rod: (a) STEM picture; (b) results of 50 EDX analyses obtained through automatic stepping of the beam along the line marked on STEM picture.

ing grain boundaries (i.e. recrystallization fronts), large particles can dissolve completely. The original large particles are therefore observed before the grain boundary (migrating front) and disappear behind it.

If a ST-sample is deformed at intermediate temperature, dynamic precipitation operates in the large-particle-free area.

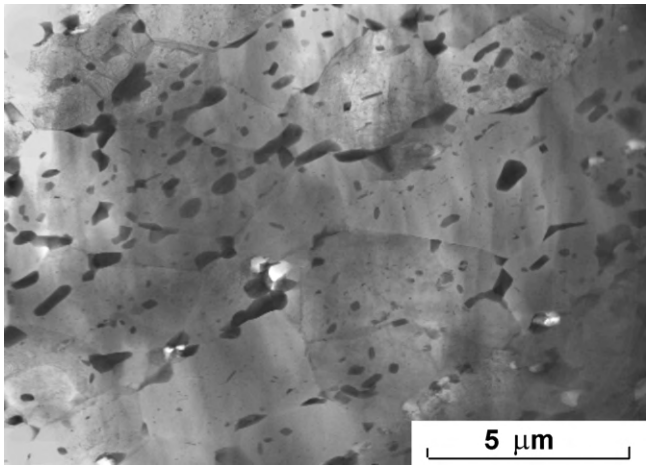

Fig. 7. Structure of the rod extruded by means of oscillating die (KOBO) method (STEM).

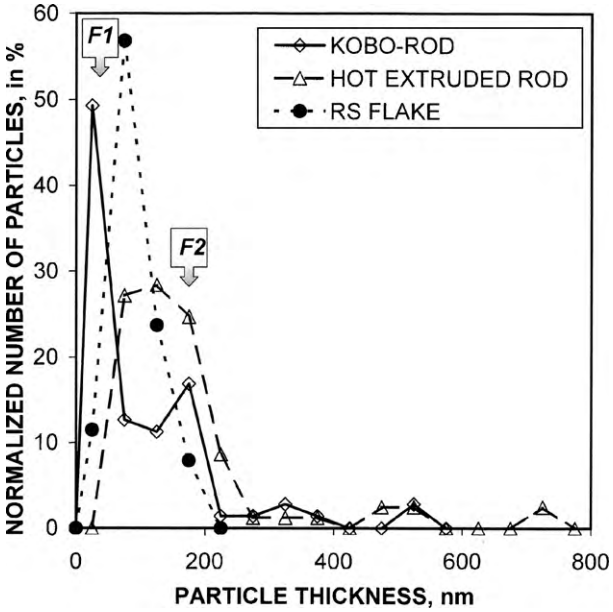

Fig. 8. Normalized distribution of the particle size for RS flake, hot-extruded rod (direct extrusion at ~673 K), and KOBO-extruded rod (lengthwise dimensions of the particles were measured).

Within the area containing large particles, re-coarsening of the remaining particles is probably responsible for the depreciation of Zn-content in the neighboring matrix, and, in consequence, suppresses the nucleation of fine η' and η particles in the vicinity of pre-existing large particles.

The mentioned structural effects are in accordance with the evidently suppressed hardening of the hot-deformed ST-material. It is worth emphasizing that the flow stress increase due to dynamic precipitation was often observed for ST-materials, as reported for other precipitation–hardenable alloys [38,39]. For the purpose of comparison, hot compression test results for the industrial 7N01 alloy (AA7000 series) are displayed in Fig. 2b. The samples were machined from an as-extruded 7N01alloy, with the composition: Al–4.4%Zn, 1.4%Mg, 0.4%Mn, 0.6%Fe [32]. The flow stress vs. deformation temperature dependence decreased monotonically (fine line no. 3). However, flow stress was found to increase efficiently at 400–450 K for solution-treated samples. A "hump" on the $\sigma_m - T^{-1}$ curve was attributed to the dynamic precipitation effect (see: dotted line no. 4).

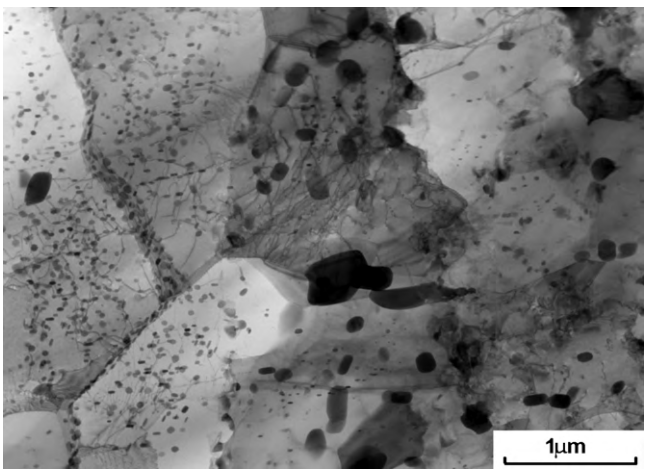

Fig. 9. Structure of ST-sample deformed at 573 K (STEM).

5. Conclusions

1. Rapid solidification of zinc-rich aluminum alloy Meso10 (AA7000 series) results in the development of fine Zn(Mg,Cu)-rich particles. The morphology of particles in RS-flakes suggests a eutectic structure rather than any structures typical of as-aged AA7000 materials, which are formed during decomposition of over-saturated solid solutions and the ensuing growth of η' and η precipitates. The precipitates observed in RS-flakes have a complex structure. However, a detailed description of their crystallographic features requires extended TEM and HREM observations and more detailed analysis. During annealing at 673–773 K, the particles transform to η and T-phases that are typical for over-aged AA7000 materials.
2. The *solvus* temperature, estimated from DSC tests at constant heating/cooling rate of 30 K/min, was found to be ~738 K and ~754 K for heating and cooling tests, respectively. It was concluded that solution treatment at a temperature higher than 754 K by ~20 K should result in the dissolution of preliminary Zn-rich particles. However, solution treatment at 773 K/30 min was found to be insufficient to cause complete particle dissolution. Incomplete dissolution of hardening particles during solution treatment is often accepted in industrial practices to avoid abnormal grain coarsening. The remaining particles in ST-samples prevent the recrystallization of formerly deformed material. However, local differences in particle size, observed for the tested material, which mostly result from different solidification rates of particular RS-flakes, can affect the annealing time that is necessary for the dissolution of particles in a given area of the structure. Therefore, at specific time/temperature conditions, small particles in one area may be dissolved completely, whereas some residuals of the originally large particles may remain undissolved in another area.
3. The above-mentioned inhomogeneity of particle distribution in ST-material resulted in negligible dynamic precipitation–hardening of ST-material, while it was being deformed at intermediate deformation temperatures. Fine particles responsible for the strengthening of the material were observed at locally recrystallized grains. Within the area containing residuals of preliminary particles, precipitation–hardening was negligible. The coarsening of preliminary particles during ageing "consumed" the excess of solutes from the surrounding over-saturated matrix and resulted in a suppressed hardening effect that is usually caused by homogeneous nucleation of very fine particles.

Acknowledgements

The authors are very grateful to Professor Junichi Kaneko for his remarkable contribution to the research project and valuable discussion of results. Prof. Wlodzimierz Bochniak's assistance in KOBO extrusion experiments is kindly acknowledged.

References

[1] G.E. Totten, D.S. Scott MacKenzie (Eds.), Physical Metallurgy and Processes in Handbook of Aluminum, vol. 1, Marcel Dekker Inc., New York, Basel, 2003.
[2] K. Seimiya, M. Sugamata, L. Blaz, J. Kaneko, J. Japan Soc. Powder Powder Metall. 53 (2006) 899.
[3] J. Kaneko, M. Sugamata, L. Blaz, R. Kamei, Mater. Sci. Forum 396–402 (2002) 161.
[4] L. Blaz, M. Sugamata, J. Kaneko, J. Sobota, G. Wloch, W. Bochniak, A. Kula, J. Mater. Process. Technol. 209 (2009) 4329.
[5] K. Raju, S.N. Ojha, A.P. Harsha, J. Mater. Sci. 43 (2008) 2509.
[6] R. Dasgupta, J. Mater. Process. Technol. 72 (1997) 380.
[7] P.J. Ward, H.V. Atkinson, P.R.G. Anderson, L.G. Elias, B. Garcia, L. Kahlen, J.-M. Rodriguez-Ibabe, Acta Mater. 44 (1996) 1717.
[8] T. Laha, A. Agarwal, T. McKechnie, K. Rea, S. Seal, Acta Mater. 53 (2005) 5429.
[9] L. Blaz, A. Kula, J. Kaneko, M. Sugamata, G. Wloch, K. Sobota, J. Microsc. 237 (2010) 416.
[10] B.-C. Ko, Y.-C. Yoo, Compos. Sci. Technol. 59 (1999) 775.
[11] W.L. Zhang, J.X. Wang, D.Z. Wang, M.Y. Gu, J. Mater. Sci. 40 (2005) 6091.
[12] X.N. Zhang, L. Geng, G.S. Wang, J. Mater. Process. Technol. 176 (2006) 146.
[13] X.N. Zhang, L. Geng, B. Xu, Mater. Chem. Phys. 101 (2007) 242.
[14] M. De Sanctis, Mater. Sci. Eng. A141 (1991) 103.
[15] E. Salamci, R.F. Cochrane, Mater. Sci. Technol. 18 (2002) 1445.
[16] E. Salamci, R.F. Cochrane, Mater. Sci. Technol. 19 (2003) 1130.
[17] E. Salamci, Mater. Sci. Technol. 20 (2004) 859.
[18] J.D. Robson, Mater. Sci. Eng. A382 (2004) 112.
[19] D. Godard, P. Archambault, E. Aeby-Gautier, G. Lapasset, Acta Mater. 50 (2002) 2319.
[20] R. Ferragut, A. Somoza, A. Tottley, A. Torriani, J. Mater. Process. Technol. 141 (2003) 35.
[21] J. Gjonnes, C.H.R.J. Simensen, Acta Metall. 18 (1970) 881.
[22] S.P. Ringer, K. Hono, Mater. Charact. 44 (2000) 101.
[23] A.K. Mukhopadhyay, Phil. Mag. Lett. 70 (1994) 135.
[24] L.F. Mondolfo, N.A. Gjostein, D.W. Levinson, J. Metall. Trans. AIME (1956) 1378.
[25] L.K. Berg, J. Gjonnes, V. Hansen, X.Z. Li, M. Knutson-Wedel, G. Waterloo, D. Schryvers, L.R. Wallenberg, Acta Mater. 49 (2001) 3443.
[26] W. Bochniak, A. Korbel, Mater. Sci. Technol. 16 (2000) 664.
[27] W. Bochniak, A. Korbel, J. Mater. Process. Technol. 134 (2003) 120.
[28] W. Bochniak, A. Korbel, Mater. Sci. Forum 331-3 (Part 1–3) (2000) 613.
[29] K.U. Kainer, Metal Matrix Composites, WILEY-VCH Verlag GmbH & Co. KgaA, 2006.
[30] J.M. Papazian, Metall. Trans. 13A (1982) 761.
[31] C.-Y. Shieu, S.-J. Lin, J. Mater. Sci. 32 (1997) 1741.
[32] A. Kula, L. Blaz, J. Koziel, M. Sugamata, G. Wloch, Problems of Modern Techniques in Engineering and Education–2008, Pedagogical University of Cracow, 2008, 63.
[33] T.S. Srivatsan, T.S. Sudarshan, E.J. Lavernia, Prog. Mater. Sci. 39 (1995) 317.
[34] R. Trivedi, F. Jin, I.E. Anderson, Acta Mater. 51 (2003) 289.
[35] T. Fujiwara, T. Ogawa, Solid-State Science, Springer-Verlag, Heidelberg, 1990, 93.
[36] M. Senechal, Quasicrystals and Geometry, Cambridge Univ. Press, 1995.
[37] R. Divakar, D. Sundararaman, V.S. Raghunathan, Prog. Crist. Growth Charact. 34 (1997) 263.
[38] L. Blaz, E. Evangelista, Mater. Sci. Eng. A207 (1996) 195.
[39] L. Blaz, A. Korbel, W. Bochniak, Z. Rdzawski, in: Y. Hosoi, et al. (Eds.), Proc. 7th JIM Intern. Symp. (JIMIS7), The Japan Institute of Metals, Nagoya – Japan, 1993, p. 287.
[40] M. Gremaud, D.R. Allen, M. Rappaz, J.H. Perepezko, Acta Mater 44 (7) (1996) 2669–2681.